Soft Matter

Accepted Manuscript

Volume 12 Number 1 7 January 2016 Pages 1–314

Soft Matter

www.softmatter.org

ISSN 1744-683X

ROYAL SOCIETY OF CHEMISTRY

PAPER
Jure Dobnikar et al.
Rational design of molecularly imprinted polymers

175 YEARS

ROYAL SOCIETY OF CHEMISTRY

rsc.li/soft-matter-journal

Soft Matter

ARTICLE TYPE

Assembly of three-dimensional binary superlattices from multi-flavored particles[†]

Evan Pretti,[a] Hasan Zerze,[a] Minseok Song,[a] Yajun Ding,[a] Nathan A. Mahynski,[b] Harold W. Hatch,[b] Vincent K. Shen,[b] and Jeetain Mittal[*a]

Binary superlattices constructed from nano- or micron-sized colloidal particles have a wide variety of applications, including the design of advanced materials. Self-assembly of such crystals from their constituent colloids can be achieved in practice by, among other means, the functionalization of colloid surfaces with single-stranded DNA sequences. However, when driven by DNA, this assembly is traditionally premised on the pairwise interaction between a single DNA sequence and its complement, and often relies on particle size asymmetry to entropically control the crystalline arrangement of its constituents. The recently proposed "multi-flavoring" motif for DNA functionalization, wherein multiple distinct strands of DNA are grafted in different ratios to different colloids, can be used to experimentally realize a binary mixture in which all pairwise interactions are independently controllable. In this work, we use various computational methods, including molecular dynamics and Wang-Landau Monte Carlo simulations, to study a multi-flavored binary system of micron-sized DNA-functionalized particles modeled implicitly by Fermi-Jagla pairwise interactions. We show how self-assembly of such systems can be controlled in a purely enthalpic manner, and by tuning only the interactions between like particles, demonstrate assembly into various morphologies. Although polymorphism is present over a wide range of pairwise interaction strengths, we show that careful selection of interactions can lead to the generation of pure compositionally ordered crystals. Additionally, we show how the crystal composition changes with the like-pair interaction strengths, and how the solution stoichiometry affects the assembled structures.

1 Introduction

Nano- or micron-sized colloidal particles can undergo self-assembly to form binary nanoparticle superlattices (BNSLs)[1–3], which have a number of useful material design applications. For colloidal crystals in general, notable applications include photonics[4,5], sensing[6,7], and catalysis[8,9]. By controlling the relative sizes of colloidal particles in binary systems and the nature of their interactions, a myriad of structures have been produced experimentally from self-assembly: CsCl, NaCl, CuAu, NaTl, AlB$_2$, MgZn$_2$, Cr$_3$Si, Cu$_3$Au, Cs$_6$C$_{60}$, and others[2,3,10–15]. The interactions between the two components of a BNSL may be realized by

Coulombic forces[2,16], although more complex schemes can also be employed to precisely tune attractive and repulsive interactions between particles. It is generally more difficult to tune the resulting structure using only energetic interactions without exploiting size asymmetry, as entropic packing effects are a powerful driving force for self-assembly of BNSLs.[17]

One way to promote the self-assembly of colloidal particles is through functionalization of their surfaces with DNA[12,13,18,19]. DNA-functionalized particles (DFPs) interact with each other through complementary Watson-Crick base-pairing interactions (see Fig. 1A), and have been used to assemble a number of BNSL structures[20–24]. Despite an abundance of studies on the self-assembly of DNA-functionalized nanoparticles, micron-sized systems have been investigated to a much more limited extent due primarily to experimental difficulties. In particular, for micron-sized particles, because the interactions are very short-ranged relative to the particle sizes, long and tedious annealing stages are required. Furthermore, these systems generally exhibit an extremely narrow melting transition range on the order of 1-2

[a] Lehigh University, Chemical and Biomolecular Engineering, 111 Research Dr., Bethlehem, Pennsylvania 18015-4791, USA. Fax: (610) 758-5057; Tel: (610) 758-4791; E-mail: jeetain@lehigh.edu

[b] Chemical Sciences Division, National Institute of Standards and Technology, Gaithersburg, Maryland 20899-8320, USA.

[†] Electronic Supplementary Information (ESI) available: Structural analysis details, melting curves, and supplementary simulation results including time dependent data. See DOI: 10.1039/b000000x/
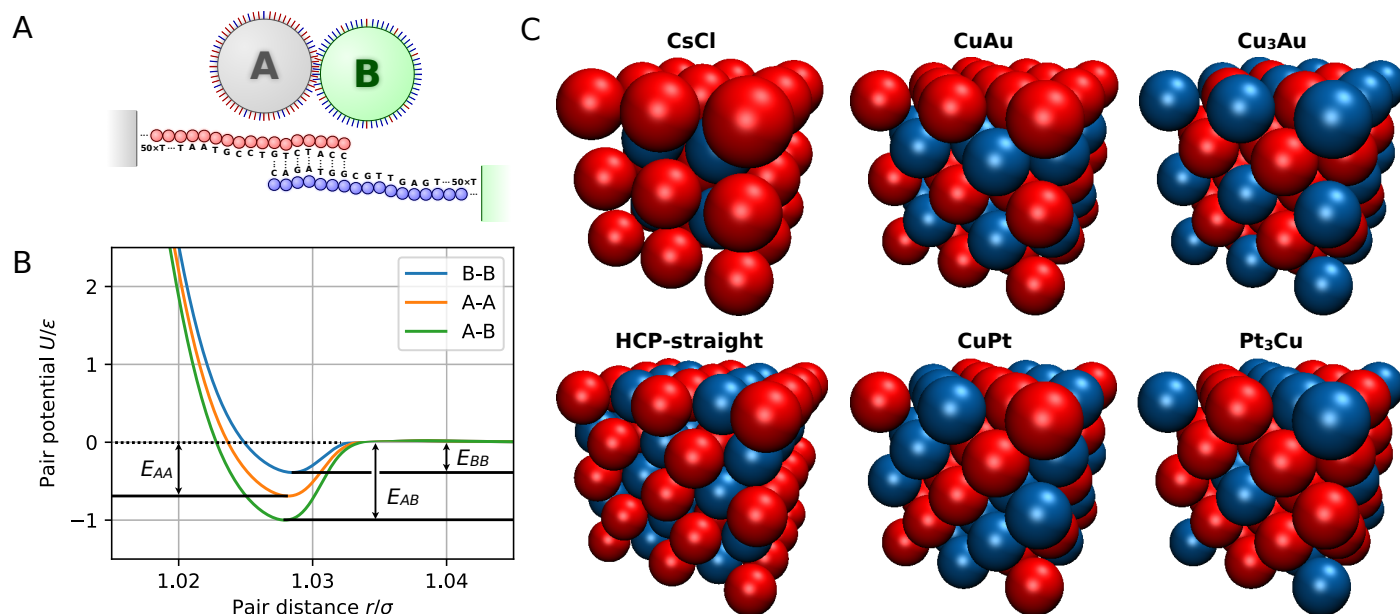
Soft Matter Accepted Manuscript

Fig. 1 Multi-flavoring of colloidal particles *via* DNA functionalization. (A) Schematic representation of the two types of particles in a multi-flavored system having different fractions of complementary single-stranded DNA sequences. (B) Each of the pairwise attraction strengths E_{AA}, E_{BB}, and E_{AB} can be manipulated experimentally by controlling the grafting densities of the DNA sequences, and in the simulated implicit model by changing the parameters of the (illustrated) effective pair potential. (C) Compositionally ordered binary structures of interest, including BCC CsCl, "HCP-straight", and FCC CuAu, CuPt, Cu_3Au, and Pt_3Cu.

°C.[20,23,25–27] The latter may be somewhat ameliorated by exploiting re-entrant melting or DNA strand displacement methods to extend the range of the melting transition.[28,29] Such developments have improved the appeal of micron-sized systems, which have especially advantageous optical properties[30] and are relatively easy to observe using confocal microscopy.[31–33]

Typically, selective binding between DNA molecules tethered on two different particles is achieved in one of two ways. First, complementary single-stranded DNA (ssDNA) may be grafted on different particles so that they bind through direct hybridization with each other[34]. Alternatively, this may be done indirectly by grafting the same ssDNA on both particles, and then introducing a complementary linker that can hybridize with the strands on both particles[35]. Consequently, the unlike pairs effectively attract each other, whereas non-complementary like pairs repel each other due to steric interactions. In both instances, the interactions between like and unlike DFPs are not entirely independent of each other.

As a means of achieving this independence, it has recently been suggested that particles can be functionalized with a blend of two types of DNA strands with complementary concentrations on each particle. These "multi-flavored" particles can exhibit a tunable attraction between the like particles while maintaining the interaction between unlike pairs. Indeed, this approach has been shown to induce the crystallization of equally sized particles into body-centered cubic (BCC) and close-packed (CP) superlattices, *i.e.*, the hexagonal close-packed (HCP) and face-centered cubic (FCC) structures.[36,37] In this instance, the like and unlike interactions may be tuned independently; however, each like interaction is not independent of the other because the relative concentrations of the two strands are fixed.

As an extension of this multi-flavored motif, it has been proposed that by controlling the relative composition of each strand on different particles, the like interactions of each species can be tuned independently.[38,39] For example, in a system composed of "A" and "B" particles, the A-A and B-B interactions are no longer required to be identical (see Fig. 1B). This increases the design parameter space and is expected to open new avenues for the self-assembly of DFPs. Previous investigation into the self-assembly of two-dimensional multi-flavored nanoscale colloids revealed that their morphologies could be rationalized on the basis of energetic arguments.[40] However, three-dimensional micron-scale systems remain largely unexplored systematically. Furthermore, many studies of binary DFP systems focus on cases where size disparity between the system components is used in addition to interparticle interactions to drive the assembly towards desired structures. Size asymmetric systems rely greatly on entropic packing effects to assist in determining the relative locations of different constituents, *i.e.*, which type of particle exists in the interstices between the other, effectively making certain lattice sites distinguishable from one another. Equally sized particles, however, cannot leverage such a benefit, and must therefore be energetically driven into an ordered structure since all sites are essentially identical to each particle undergoing assembly. The diversity of, and the ability to robustly assemble, structures resulting from the self-assembly of three-dimensional multi-flavored micron-sized particles with equal sizes remains an outstanding question which we seek to address.

In this work, we use various computational methods to study the self-assembly of multi-flavored micron-sized DFPs into different three-dimensional superlattices by manipulating their interparticle interactions. Examples of these superlattice structures

are shown in Fig. 1C; we considered an extensive list of structures and found the ones shown to be of particular interest for this system based on our simulation results, energetic calculations, and observations that these structures should be mechanically stable when constructed from size-symmetric particles. Inspired by experimental approaches, we treat the unlike (A-B) interaction as fixed, which defines the characteristic energetic interaction scale of the system, while the two like interactions (A-A and B-B) are tuned independently. We investigate both the ground state (zero temperature limit) and finite temperature cases to examine the consequence of entropy on the capacity of ground state theories to reasonably predict the outcome of self-assembly. In Sec. 2, we present the details of the computational models and approaches we have employed here. The results of our molecular dynamics simulations and corresponding rationale using energy minimization calculations and flat-histogram Monte Carlo simulations are subsequently discussed in Sec. 3.

2 Methods

2.1 Micron-sized multi-flavored DFPs

Fig. 1A shows a schematic representation of how multi-flavored DNA-functionalized micron-sized particles interact with each other, while Fig. 1B indicates how the strengths of attractive interactions E_{AA}, E_{BB}, and E_{AB} between different pairs of particles can be adjusted independently. This "asymmetric" multi-flavoring strategy [38,39] is a generalization of the multi-flavoring strategy originally proposed by Crocker and coworkers [36,37], in which the like-pair interactions E_{AA} and E_{BB} may not differ from each other. Previous explicit-chain simulations and experimental studies of micron-sized DFPs [39,41] have shown that their interactions can be characterized by short-ranged pair potentials. Such a simple pairwise approach to modeling DFP interactions will be inaccurate for nanoscale particles due to multi-body effects [42]. However, the interactions between the micron-sized particles considered here have very short ranges compared to the diameters of the particles themselves (note that the abscissa of Fig. 1B is to scale for particles having core diameters $\approx \sigma$), so pair potentials should suitably describe the interactions in this system.

The functional form of the pair potential used in this study is that of a Fermi-Jagla potential: [43], which has been used successfully to study the self-assembly of multi-flavored micron-sized DFPs in two dimensions [39]:

$$\frac{U(r/\sigma)}{\varepsilon} = \left(\frac{\varepsilon_c}{\varepsilon}\right)\left(\frac{\sigma_c/\sigma}{r/\sigma - R_s/\sigma}\right)^n +$$

$$\frac{A_0/\varepsilon}{1 + \exp[A_1(r/\sigma - A_2)]} - \frac{B_0/\varepsilon}{1 + \exp[B_1(r/\sigma - B_2)]} \quad (1)$$

The first term in this equation models the particle core-core repulsion using an nth-power inverse distance relationship, where ε_c is the energy scale of the repulsion, σ_c is the length scale controlling the range of the repulsion from the colloid surface, and R_s is a shifting factor related to the colloid size. The second and third terms containing the exponentials capture the repulsion of DNA strands due to steric effects, and attraction due to hybridization of

complementary DNA sequences, respectively. In these terms, A_0 and B_0 control the strengths of these interactions, A_1 and B_1 control their ranges, and A_2 and B_2 control the separation distances at which they occur.

The values of the parameters which are appropriate for modeling DNA-mediated interactions are taken from previous studies of self-assembly of binary systems of DFPs in two dimensions [39] (cf. ESI† for details). All parameters in the equation remain fixed, except for the attractive energy scale B_0, which is varied to control the depth of the attractive well E_{ij} (Fig. 1B directly illustrates the behavior of Eq. 1 for various values of B_0). Since interactions between all pairs of particle types are independently tunable, this leaves three controllable interaction energies E_{AA}, E_{BB}, and E_{AB}. For normalization purposes, we let $E_{AB} = \varepsilon$ and study the effects of varying the relative attraction strengths E_{AA}/E_{AB} and E_{BB}/E_{AB} between 0 and 1. Note that setting $E_{AA}/E_{AB} = E_{BB}/E_{AB} = 0$ reduces the system to one matching a "single flavored" DFP system, and setting $E_{AA}/E_{AB} = E_{BB}/E_{AB} = 1$ reduces it to an effectively unary system in which pairwise interactions between all particle types are identical.

2.2 Molecular dynamics

We used the LAMMPS package [44] to perform molecular dynamics (MD) simulations in the canonical ensemble. Unless otherwise specified, the systems consisted of mixtures of 500 total particles with 1:1, 2:1, or 3:1 ratios of A-type and B-type particles having equal masses. The particles were size-symmetric, with diameters approximately equal to 1 σ (cf. Sec. 2.1 and the ESI† for information about the pair potentials employed). Simulations were conducted within a periodic cubic box sized such that the number density $\rho = 0.02\ \sigma^{-3}$. A Langevin thermostat was applied with a time constant $\tau = 2\ \sigma m^{1/2}\varepsilon^{-1/2}$, and the simulation time step was set to $\Delta t = 10^{-3}\ \sigma m^{1/2}\varepsilon^{-1/2}$. The starting configuration for each simulation was a random arrangement of particles in the simulation box, equilibrated for 10^6 steps at $T = 1\ \varepsilon k_B^{-1}$ using a purely repulsive Weeks-Chandler-Andersen potential [45] to eliminate particle overlaps. Each system was then equilibrated using the potential of Eq. 1 with the desired parameters for an additional 10^6 steps, and then run for 3×10^8 steps at a lower temperature. 5 replicate simulations, starting from unique initial conditions, were completed for each set of parameters. Example snapshots illustrating the nature of the initial configurations and the progression of the simulations are provided in Fig. S1 (ESI†).

To allow the systems to anneal in a reasonable amount of time, we chose each simulation temperature to be near the putative system melting temperature T_m, which ranged from 0.125 εk_B^{-1} to 0.165 εk_B^{-1} depending on the values of E_{AA}/E_{AB} and E_{BB}/E_{AB} used. To estimate T_m for each system, we performed additional cooling simulations in which the temperature was lowered from $T = 0.20\ \varepsilon k_B^{-1}$ to $T = 0.05\ \varepsilon k_B^{-1}$ at a constant rate of $dT/dt = -1.5 \times 10^{-7}\ \varepsilon^{3/2} m^{-1/2} k_B^{-1} \sigma^{-1}$. See Fig. S2 (ESI†) for system melting temperatures, a representative melting curve obtained during a cooling simulation, and a demonstration of the independence of the melting temperature from the size of the system simulated.
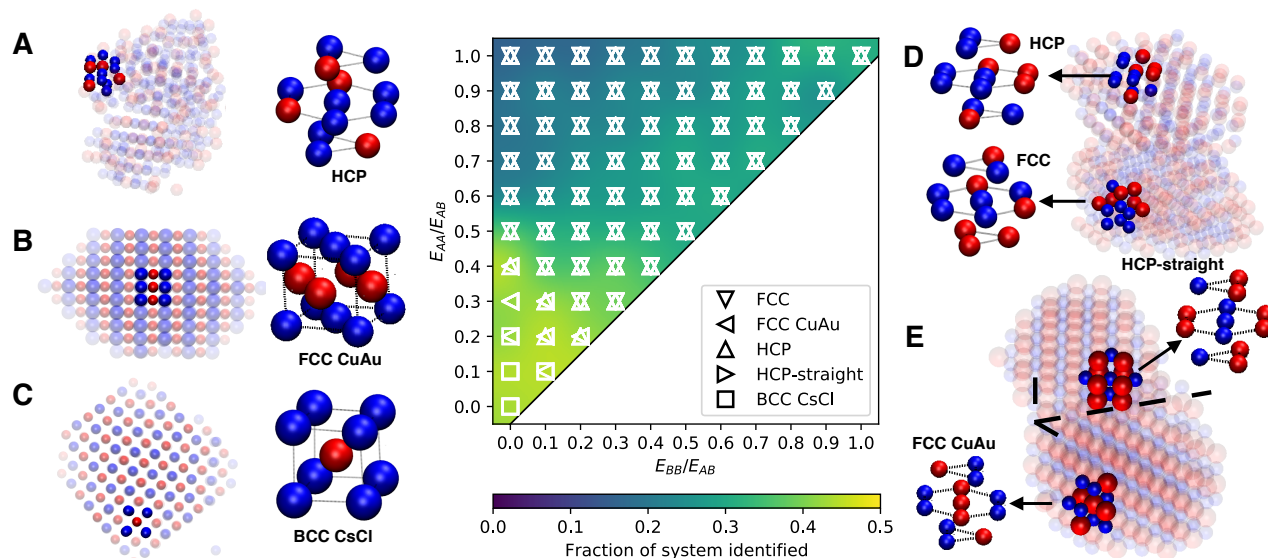
Fig. 2 Order diagram of the crystals grown in our MD simulations as a function of E_{AA}/E_{AB} and E_{BB}/E_{AB} near their respective putative melting temperatures. Since the two types of particles are present in a 1:1 ratio and their diameters are equal, particle identities may be exchanged and the diagram can be made symmetric about the $E_{AA}/E_{AB} = E_{BB}/E_{AB}$ line. Symbols show structures observed within individual simulations and across replicate simulations. The heatmap shows the fraction of particles conclusively identified by CNA (see Sec. 3.1 for a discussion of this parameter). The example crystals shown are taken from simulations at (A) $E_{AA}/E_{AB} = 1$, $E_{BB}/E_{AB} = 0$, (B) $E_{AA}/E_{AB} = 0.3$, $E_{BB}/E_{AB} = 0$, (C) $E_{AA}/E_{AB} = E_{BB}/E_{AB} = 0$, (D) $E_{AA}/E_{AB} = E_{BB}/E_{AB} = 1$, and (E) $E_{AA}/E_{AB} = E_{BB}/E_{AB} = 0.2$.

Trajectories generated from the isothermal simulations were inspected visually using Visual Molecular Dynamics (VMD)[46] to check for crystal formation. The Open Visualization Tool (OVITO)[47] Python interface was used to perform cluster size and composition analysis, as well as common neighbor analysis (CNA)[48–50] to identify the structural and compositional order of the crystals. The algorithms employed by OVITO are not capable of identifying particles on the surfaces of clusters, and as a result, some particles whose structural order is considered "unclassifiable" actually lie on the surfaces of ordered clusters. Since we are more concerned in this work with relative fractions of various structures, structural and compositional order results have been normalized accordingly. See the ESI† for more information about the CNA implementation details.

2.3 Wang-Landau simulations

Wang-Landau (WL) simulation is a flat-histogram method which computes the probability distribution of the macrostates of a system along a given order parameter.[51,52] The inverse of this distribution is used to bias the simulation such that the macrostates are visited with close to equal probability. In particular, here, we performed temperature-expanded WL simulations with the FEASST software package[53] to sample compositional order as a function of temperature for different stoichiometries (AB, A_2B and A_3B), different lattices, (BCC, FCC and HCP), and different pair interaction energies (values of E_{AA}/E_{AB} and E_{BB}/E_{AB}.)

For each simulation, the initial configuration was a perfectly ordered lattice with particle identities randomly assigned to generate compositionally disordered structures. To span the temperature space, we used 21 grid points between $T_{\min} = 0.05 \ \varepsilon k_B^{-1}$ and $T_{\max} = 1 \ \varepsilon k_B^{-1}$ such that values of $1/T$ were equally spaced. We

performed identity swap moves, anisotropic volume relaxation moves at zero pressure, and changes in temperature, in a ratio of 10000:300:1. We used a total of 40 sweeps for each WL simulation, corresponding to the number of times the visited-states histogram was found to be flat, *i.e.* when the Wang-Landau f parameter was reduced by half. No information for accumulating averages was recorded during the first 15 WL sweeps. The simulation was checked for "flatness" every 10^5 MC steps.

3 Results and discussion

3.1 Molecular dynamics

The molecular dynamics simulations configured as described in Sec. 2.2 were performed to study the self-assembly process in the presence of enthalpic, entropic and kinetic factors. We intentionally chose the constant volume ensemble and low number density to capture the effects of only the driving forces of experimental relevance during self-assembly. These low density systems, in which the pressure is essentially zero, are reflective of conditions in which formed crystals are surrounded by only a dilute vapor of single particles. These conditions give rise to assembly driven only by the interactions between particles, rather than also by packing effects. Polydisperse particle systems have been considered in other studies[1,10,16,38], showing how particle size asymmetry can drive the creation of ordered lattices in three dimensions. However, we are interested in the self-assembly behavior of size-symmetric systems, in which enthalpic driving forces predominate, as there is a relatively limited understanding of the behavior of these systems.[39]

Results from these simulations are presented in Fig. 2. Symbols shown in the order diagram are structural classifications given by common-neighbor analysis (CNA, detailed in Sec. 2.2), while the

heatmap indicates the average fraction of particles for each replicate simulation run identified by CNA as a part of an ordered structure. The appearance of multiple symbols at a single point can indicate either polymorphism within individual runs, or the presence of different structures across replicate runs. The quantitative behavior of the appearance of multiple phases in Fig. 2 is shown in Fig. 3A for the diagonal of Fig. 2, and in Fig. 3B for its vertical axis. In this presentation, the range of different system compositions found across replicate simulations is captured by the error bars. Compositionally disordered FCC and HCP structures are indicated as "unidentified," reflecting that CNA was able to detect structural but not compositional order in the crystals produced. Note that the results of Figs. 2 and 3 do not necessarily indicate that thermodynamic coexistence is present between multiple identified phases, or that the formed phases are thermodynamically favorable at the simulated conditions. Instead, they show the actual products of self-assembly accounting for the dynamics of the assembly process; these products may be kinetically trapped.

Although the amounts of identified particles are low relative to the total amounts present in the simulations, there are a few different situations which can prevent CNA from identifying particles. For instance, a particle may be part of a large ordered crystal, but may be located on its surface, in which case CNA will not be able to properly determine the crystal structure based only upon local information about the particle's neighbors. On the other hand, the particle may be a part of an ordered structure absent from the list of structures for which CNA is searching. Finally, a particle may actually exist in isolation, in a very small cluster, or in a large but disordered cluster. In such cases CNA should, by design, indicate that such a particle is not part of an ordered structure.

In this work, we are only interested in establishing qualitative trends for the relative amounts of various structures formed. Thus, the inability of CNA to identify surface particles is not a primary concern, even though this effect can substantially reduce the fraction of particles identified overall. Other similar studies[36,54] employing CNA do not make attempts to identify particles on the surfaces of simulated clusters either. As for reliably identifying particles in the interiors of clusters, the energy analysis discussed later in Sec. 3.2 provides a list of structures out of a large library which could be expected to form in simulation. This serves as a good starting point to make sure that no candidates are missing from the list provided to CNA, and as the parameter space of the simulations is relatively small, visual inspection of trajectories at selected points within it suffices to verify that no other structures have been overlooked. These inspections also verified that the systems were assembling into crystals, and that the low fractions of particles identified as shown in Fig. 2 are mostly the result of unidentified surface particles. We found that, for most systems, the overall degree of structural order was quite high. Some simulation snapshots in addition to those in Fig. 2 illustrating crystallinity are available for reference in ESI† Figs. S1 and S3. To further confirm the presence of structural order in the systems, we generated radial distribution functions, which are illustrated for selected systems in Fig. S3 (ESI†).
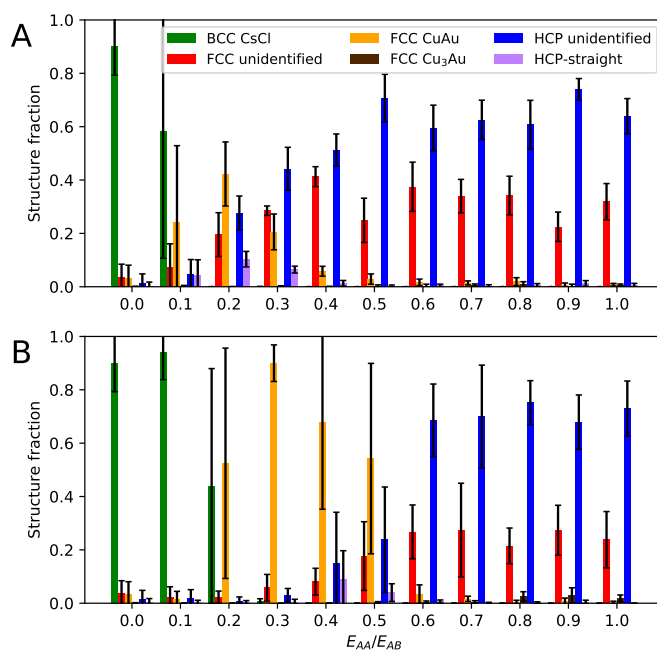

Fig. 3 Structural and compositional order data for two specific paths through the parameter space: (A) $E_{BB}/E_{AB} = E_{AA}/E_{AB}$, along the diagonal of Fig. 2, and (B) $E_{BB}/E_{AB} = 0$, along its vertical axis. Structure fractions shown here are normalized to the total fraction of identified particles. Error bars show variation across 5 sets of replicate simulations. Small amounts of CuPt and Pt$_3$Cu (see Fig. 1C) were identified but are not shown here as their fractions never exceeded 3%.

Consider first the origin of the order diagram in Fig. 2, at $E_{AA}/E_{AB} = E_{BB}/E_{AB} = 0$. No attractive interaction is present between like particles, and this case corresponds to the single-flavored DNA functionalization scheme. In agreement with prior experimental and computational results,[22,23,36,37], and as expected given that like particle contacts are purely repulsive in this scenario, BCC CsCl is formed as shown in Fig. 2C. In fact, CsCl formation has been observed in binary DNA-functionalized nanoparticle[55,56] and binary charged colloid[2,57] systems with interactions longer in range but otherwise similar in nature to the ones considered here.

Moving along the diagonal axis of Fig. 2, the attraction strengths between like particle pairs A-A and B-B are increased at an equal rate. These systems can be realized using DFPs with a symmetric multi-flavoring approach. Relative fractions of various identified structures for this case are given in Fig. 3A. As E_{AA}/E_{AB} and E_{BB}/E_{AB} increase, mixtures of various close packed structures are observed. Fig. 2E shows grains of HCP-straight and FCC CuAu at $E_{AA}/E_{AB} = E_{BB}/E_{AB} = 0.2$. For $E_{AA}/E_{AB} = E_{BB}/E_{AB} > 0.2$ up to the limiting case of $E_{AA}/E_{AB} = E_{BB}/E_{AB} = 1$ in which all interparticle interactions are identical, compositionally disordered HCP and FCC form. This can be explained by noting that as the difference between like and unlike particle interactions decreases, the enthalpic penalty for forming compositionally disordered structures decreases. When E_{AA} and E_{BB} are significantly smaller than E_{AB}, there is a relatively large penalty for the presence of a like-pair contact in the place of an unlike-pair contact. Therefore,
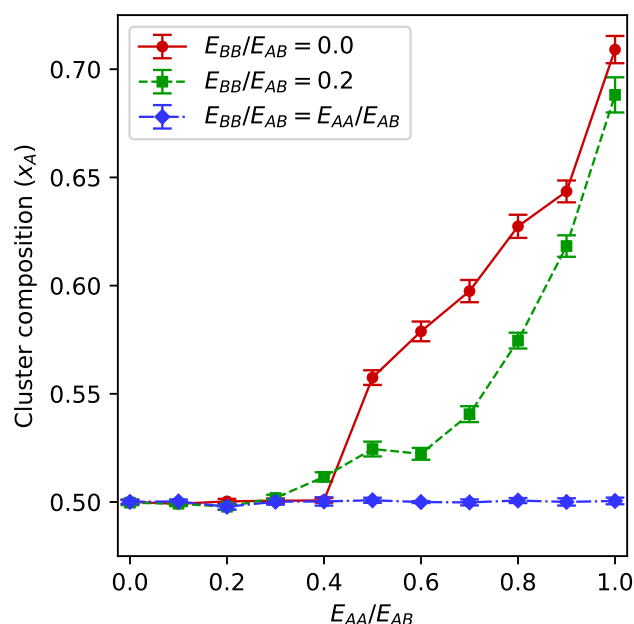
Fig. 4 Effects of varying E_{AA}/E_{AB} on cluster composition in MD simulations. Solution stoichiometry is 1:1. Three cases for values of E_{BB}/E_{AB} are shown. For a given point, composition of the largest cluster is averaged over the last 50% of a simulation.

there exists a large penalty for a defect in a compositionally ordered lattice in which, for example, an A-type particle occupies a site where a B-type particle should be present. On the other hand, if E_{AA} and E_{BB} are close to E_{AB}, there is only a small penalty to compositional disorder, and finite temperature effects may overcome the enthalpic barrier.

It can be seen from Fig. 3 that the formation of HCP, albeit compositionally disordered, is favored at larger like pair attraction energies. However, we have not found it possible to consistently generate single pure crystals other than CsCl in this symmetric case. Our results along the diagonal for the formation of BCC and FCC structures are consistent with the results of Casey *et al.*[36], in which CsCl, CuAu, and disordered FCC phases are reported. Their data indicate, with increasing E_{AA}/E_{AB}, that CuAu formation begins near $E_{AA}/E_{AB} \approx 0.12$, and that compositionally disordered FCC is observed beyond $E_{AA}/E_{AB} \approx 0.39$. Note that their experimental results do not directly indicate observation of HCP structures, although they do report "HCP-like stacking faults" in their formed FCC crystals. Inspection of their simulation results ultimately shows somewhat similar behavior to that of our system, in which HCP appears along with FCC. The appearance of these two structures together is not surprising, as the nearest neighbor environments of these structures are identical and, as discussed later in Sec. 3.2, the compositionally ordered CuAu FCC and HCP-straight structures which we observe appearing together in our simulations are energetically degenerate.

The principle of BCC CsCl structures being favored when like-pair interactions are purely repulsive, with FCC CuAu structures forming once attraction is introduced between like pairs, holds

true in general. For instance, the results of Zhang *et al.*[24] report transformations between different binary superlattice structures created from DNA-functionalized nanoparticles (instead of the micron-sized particles considered here) which are induced by changing interparticle interactions in already assembled structures. These results consider the compositional ordering of structures formed by introducing like-pair attractions into a system initially containing only attractive interactions between unlike particle pairs. Even for this system of DNA-functionalized nanoparticles, in which interactions have longer ranges than in micron-sized systems, a switch from BCC CsCl to FCC CuAu is observed upon the introduction of this attraction.

We now consider the situation where like pair attraction energies can be independently tuned, corresponding to DFP systems using asymmetric multi-flavoring. Suppose that E_{BB}/E_{AB} is held at 0 while E_{AA}/E_{AB} is allowed to vary: in this case, type B particles always experience purely repulsive contacts between themselves, while some attraction may be present between those of type A. The molecular dynamics results are given along the vertical axis of Fig. 2, while fractions of the phases observed are presented in Fig. 3B. Naturally, for $E_{AA}/E_{AB} = 0$, this scenario is identical to the symmetric one, but differences arise as E_{AA}/E_{AB} increases. Although for $E_{AA}/E_{AB} \geq 0.6$, similar behavior is observed as in the symmetric case (compositionally disordered HCP with some FCC), significant amounts of FCC CuAu form for $0.2 \leq E_{AA}/E_{AB} \leq 0.5$, with nearly pure CuAu crystallizing at $E_{AA}/E_{AB} = 0.3$. This result was consistent across all replicate simulations performed at this condition, and as discussed later in Sec. 3.2, is surprising and unexpected from energetic considerations alone.

It might be expected that, as E_{AA}/E_{AB} is increased, the incorporation of additional A-type particles into a forming crystal should become more favorable, and that this might lead to ordered A_2B and A_3B lattices. However, such structures were not observed in the simulations shown in Fig. 2, nor were they found in additional MD simulations performed with 2:1 and 3:1 solution stoichiometries (see Fig. S4, ESI†). Notably, Cu_3Au, which was expected based on the results of energy calculations presented later in Sec. 3.2, was not seen in any substantial amount. To better understand how pairwise interactions affect the composition of the formed crystals, compositions of identified particle clusters are presented in Fig. 4. The reference symmetric multiflavoring case is shown, in which the composition never deviates from 1:1. It is accompanied with the asymmetric cases $E_{BB}/E_{AB} = 0$ and $E_{BB}/E_{AB} = 0.2$, in which the crystals become enriched in A-type particles as the A-A binding strength increases relative to the B-B binding strength.

Note how the fraction x_A never reaches the value of 3/4 (corresponding to an A_3B crystal stoichiometry) required for the formation of pure Cu_3Au. Also, for $E_{BB}/E_{AB} = 0$, it increases monotonically with increasing E_{AA}/E_{AB}, consistent with a gradual enrichment of a compositionally disordered phase with A-type particles rather than formation of, *e.g.*, an ordered A_2B phase followed by an ordered A_3B phase. From this data alone, it appears that creation of A_3B crystals from a solution with 1:1 stoichiometry is infeasible within the parameter space considered. However, these

compositions are measured after assembly is complete, and examining how apparent cluster compositions change with crystal size in Fig. S5 (ESI†) shows that crystals initially assemble with a given stoichiometry, and some excess free particles then attach themselves to crystal surfaces. For $E_{AA}/E_{AB} = 1$ and $E_{BB}/E_{AB} = 0$, the initial composition x_A is very close to the target of $3/4$. It may be possible to reach this desired state by careful tuning of the assembly temperature to control the attachment of particles to surfaces.

A study of this asymmetric multiflavoring strategy in 2D[39] successfully yielded compositionally ordered A_2B and A_3B hexagonal lattices, specifically honeycomb, kagome, and square kagome structures. The extension of this strategy to 3D studied here did not produce analogous structures. However, even though we are unable to achieve compositional *order* yet for this case in these 3D systems, we are able to obtain fairly precise control over the compositions of the created crystals using enthalpic driving forces only, without employing entropic packing effects.

3.2 Comparison with energy-based calculations

Although the MD simulation results provide insight into self-assembly behavior, they raise additional questions: what yields the selectivity for CuAu observed in the asymmetric case, and is it possible to obtain compositionally ordered structures with stoichiometries other than 1:1 as has been observed for this binary system in 2D? To understand what underlying factors are at play in the assembly process, we also carried out calculations to understand the behavior of these systems in the limit as $T \rightarrow 0$. In this case, the free energy $A = U - TS$ becomes equal to the potential energy, which can be computed by summing the contributions of the various pairwise interactions. A number of lattices were used, including CsCl, CuAu, Cu_3Au, CuPt, $CuPt_3$, and "HCP-straight," a compositionally ordered form of HCP observed in our simulations in which like particles are arranged in linear columns through the structure (see Fig. 1C). A large number of other structures (*e.g.* AlB_2, Cr_3Si, Li_3Bi) were also included in an initial screening but were found to be sufficiently high in energy as to not influence the results presented. No compositionally disordered structures were included, since entropic effects that would lead to their stabilization are absent in the zero temperature limit. Other similar techniques involving comparison of structures to determine stability have been used to study colloidal systems,[58–60] although the approach used here is chosen to be particularly simple as interactions are short-ranged and particles are symmetrically sized.

A few assumptions were made to allow for cases where the solution stoichiometry deviated from that of the crystal, *i.e.* where the relative fractions of A and B particles in the overall system were different from those in the lattice. We considered the potential energy change associated with the formation of a periodic perfect crystal having a set stoichiometry from an ideal gas mixture of colloids having a given stoichiometry, where any excess particles remaining from a stoichiometric mismatch are left in the non-interacting gas phase. The assumption of ideality is justified by the use of zero pressure in the lattice energy calculations. In the end, the total energy per particle of the system in this model
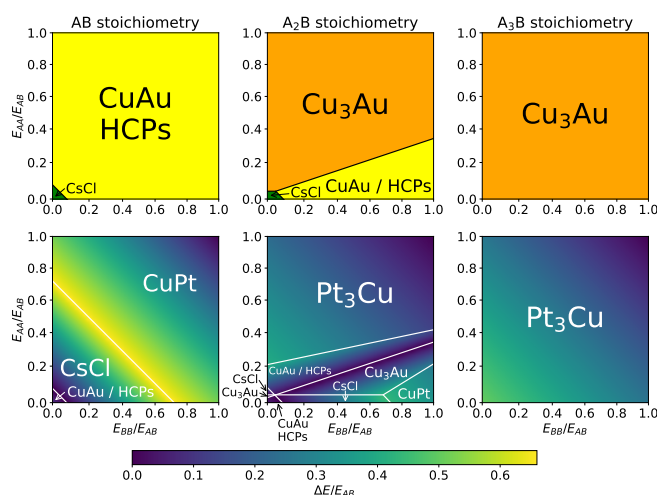

Fig. 5 Results of energy calculations over the parameter space for three different solution stoichiometries. The top row shows the most stable phases, while the bottom row shows the second most stable phases, with the shading indicating the differences in per-particle energy to the most stable phases. Note that in all cases, CuAu has identical energy to HCP-straight (designated "HCPs" in the diagram).

is:

$$U = \min\left(\frac{z_A}{x_A}, \frac{z_B}{x_B}\right)\sum_i\sum_j\int_0^{R_c} 2\pi\rho_i r^2 U_{ij}(r)g_{ij}(r)\,dr \quad (2)$$

where z_A and z_B specify the solution stoichiometry, x_A and x_B specify the crystal stoichiometry, the sums on i and j each run over particle types A and B, ρ_i is the number density of particle type i, $U_{ij}(r)$ is the pair potential for the i-j pair, $g_{ij}(r)$ is the radial distribution function (RDF) for the pair, and R_c is the cutoff radius chosen such that $|U_{ij}(R_c)/\varepsilon| < 10^{-5}$ in all cases.

To illustrate the application of this method, consider an example of the formation of Cu_3Au, a crystal structure which is 3:1 in A:B, from a solution containing a 2:1 mixture of A and B particles. In this case, the 2:1 solution stoichiometry is represented for the purpose of the calculation as $z_A = 2/3$, $z_B = 1/3$, while that of the crystal (3:1) is given by $x_A = 3/4$, $x_B = 1/4$. Now $z_A/x_A = 8/9 < 1$ while $z_B/x_B = 4/3 > 1$, indicating that particles of type A act as the limiting species in the formation of Cu_3Au, and that $8/9$ of the particles in the solution will be integrated into the lattice. The remaining $1/9$ of the total particles in the solution, all of which are excess particles of type B, remain in the non-interacting mixture and do not contribute to the total energy U.

With the stoichiometric factor determined, the energy of the lattice itself is needed. Each calculation requires the specification of a lattice represented as an orthorhombic periodic unit cell, and in this case, a set of parameters $(E_{AA}/E_{AB}, E_{BB}/E_{AB})$. The lattice is first uniformly rescaled such that the particles rest near the minima of the attractive pair potentials' wells. Then, its particle coordinates and cell volume are subjected to energy minimization using the conjugate gradient algorithm (as implemented in LAMMPS[44]), to account for small variations in the equilibrium particle positions as E_{AA}/E_{AB} and E_{BB}/E_{AB} are varied.

Results were obtained with AB, A_2B, and A_3B solution stoichiometries for comparison to MD and Wang-Landau simulation

results. The results are displayed in Fig. 5: the top row showing the most stable (lowest energy) phases, and the bottom row showing the identities of the second most stable phases as well as the differences in energy separating the two. It is important to look at this difference in energy when examining the parameter space. Even if a given phase is predicted to be stable at a given point due to its structure yielding the minimum energy, a low ΔE to the next most stable structure may lead to compositional disorder in assembled structures due to an insufficient enthalpic penalty for forming a disordered lattice.

In fact, the CuAu and HCP-straight structures have identical nearest neighbor contacts, and the short-range pair potentials used in this work cause these structures to be completely energetically degenerate. A prediction based on Fig. 5 might suggest that CuAu and HCP-straight would be formed together throughout most of the parameter space, as they are shown to form in Fig. 2E. However, it is important to remember that since compositionally disordered phases will not be predicted based on energetic considerations alone, these calculations will not predict their formation. Of course, entropic and kinetic effects play a critical role in the formation of the actual crystals observed in the MD simulations performed at finite temperatures. It is therefore not surprising to see mixtures of compositionally disordered FCC and HCP structures (*e.g.* Fig. 2D) in place of two compositionally ordered phases, especially as E_{AA} and E_{BB} grow closer to E_{AB}. In any case, the specific selectivity for CuAu in certain regions of the parameter space is not expected from energetic considerations.

Other experimental and simulation results[36,54] indicate that CuAu formation in micron-sized DFP systems may be related to diffusionless transformations from nucleated CsCl, and that the selectivity for transformation into CuAu is due to hydrodynamic effects. However, these results are given for symmetric like-pair interactions. Although we do observe CuAu formation in the symmetric case, along with some other structures, we observe the specific selectivity for the formation of pure CuAu when interactions are asymmetric. The literature results indicating that CuAu selectivity in the symmetric case is a result of hydrodynamics therefore do not rule out the possibility that our observation of CuAu in the asymmetric case is due to thermodynamic selectivity, as discussed in the following section.

As for the A_3B structures, energy calculations indicate that for an AB *solution* stoichiometry, this crystal stoichiometry is not expected. Furthermore, calculations predict that continuing to increase E_{AA}/E_{AB} at constant $E_{BB}/E_{AB} = 0$ past the range of the parameter space shown in Fig. 5 would ultimately yield pure FCC crystals of A-type particles for sufficiently large E_{AA} without ever stabilizing Cu_3Au. Now for the A_2B and A_3B solution stoichiometries, Cu_3Au is predicted to form, so its absence in the MD simulations at these stoichiometries may be due to entropic or kinetic effects. Finally, note that the energy calculations predict Pt_3Cu to be unstable, and the energies of both Pt_3Cu and $CuPt$ (whose structures are depicted in Fig. 1C) only approach those of the most stable phases in the limiting case of $E_{AA}/E_{AB} = E_{BB}/E_{AB} = 1$, when all interactions are identical and where no possibility of forming compositionally ordered phases exists.

3.3 Comparison with Wang-Landau simulations

Although the results of the energy-based calculations are revealing, they do not answer all questions about the MD simulations. To understand whether the compositional ordering behavior of the MD simulation results arises from thermodynamic or kinetic factors, Wang-Landau simulations were performed. These simulations use particle identity swaps on preset lattices, described in Sec. 2.3, allowing for the simulation of entropic effects without introducing the kinetic issues associated with crystal nucleation and growth.

Results for three lattices (BCC, FCC, and HCP) and stoichiometries (1:1, 2:1, and 3:1) are given in Fig. S6 (ESI†) for the symmetric case where $E_{BB}/E_{AB} = E_{AA}/E_{AB}$, and the asymmetric case with $E_{BB}/E_{AB} = 0$. Consider first the FCC simulations with 1:1 stoichiometry. Comparing the results for $E_{AA}/E_{AB} = 0.2$ between the symmetric and asymmetric cases, it can be seen that CuAu is more strongly favored over compositionally disordered FCC when asymmetric interactions are present. This suggests that the selectivity for CuAu seen in the MD simulations for the asymmetric case is thermodynamic, and as the energetic calculations simply predict degeneracy at these conditions, this selectivity may be an entropic effect which manifests itself at finite temperature. In general, CuAu FCC is favored over compositionally disordered FCC, whereas this is not the case with HCP-straight compared to compositionally disordered HCP. This may explain these phases' relative abundances in the MD results, where compositionally ordered lattices appearing at lower values of E_{AA}/E_{AB} are predominantly CuAu rather than HCP-straight, while the lattices which assemble for higher E_{AA}/E_{AB} values contain more compositionally disordered HCP than they do FCC.

For Wang-Landau simulations with a 3:1 stoichiometry, Cu_3Au is predicted to form from an FCC starting lattice, while no compositional order appears from HCP or BCC. Combining these results with the energetic analysis, Cu_3Au is expected to be the thermodynamically stable phase for an A_3B solution stoichiometry. This suggests that the barrier to the formation of Cu_3Au is related to the crystallization process itself. The discussion of Fig. 4 in Sec. 3.1, indicating that it should be possible to create a crystal with a 3:1 stoichiometry from a 1:1 mixture, suggests that it may even be possible to form Cu_3Au from such a mixture. However, as no appreciable quantities of Cu_3Au were seen in MD results at any of the tested stoichiometries, it may be a kinetic issue which prevents the formation of such an ordered lattice. Existing experimental results which demonstrate assembly of Cu_3Au have relied on size disparity, [3,10] so further work is needed to determine if the self-assembly conditions (such as the initial and final temperatures and the cooling rate) can be adjusted to reliably produce Cu_3Au crystals from a 3:1 mixture of size-symmetric particles.

4 Conclusions

In this work, we have shown that the self-assembly of binary systems of micron-sized DNA-functionalized particles (DFPs) can be programmed by independently tuning the two like-pair binding strengths, a requirement which can be realized with a multi-flavoring approach. We have illustrated that the results of our model match those of previous works when like-pair interactions

are symmetric, while an asymmetric multi-flavoring scheme allows for control over the composition of assembled crystals as well as selectivity for compositionally ordered structures using only particles of a single size. Although the formation of pure CsCl and CuAu crystals, for instance, is sensitive to the relative strengths of interparticle interactions, the precise tuning afforded by a multi-flavoring scheme[36] should ensure that it is possible to experimentally resolve the regions in parameter space corresponding to the desired structures. Energy-based calculations and Wang-Landau simulations provide useful insight into the factors driving the self-assembly process, suggesting that selectivity for CuAu in the asymmetric case may be thermodynamic in nature, and that kinetic barriers may stand in the way of assembly into particular A_3B structures such as Cu_3Au. In addition to tuning assembly conditions, particle size disparity, as has been used previously to assemble Cu_3Au in nanoparticle systems,[3,10] may be necessary to overcome these issues and yield such structures in micron-sized DFP systems.

Conflicts of interest

There are no conflicts to declare.

Acknowledgments

References

1　F. X. Redl, K. Cho, C. B. Murray and S. O'Brien, *Nature*, 2003, **423**, 968–971.

2　P. Bartlett and A. I. Campbell, *Phys. Rev. Lett.*, 2005, **95**, 128302.

3　M. I. Bodnarchuk, M. V. Kovalenko, W. Heiss and D. V. Talapin, *J. Am. Chem. Soc.*, 2010, **132**, 11967–11977.

4　M. B. Ross, J. C. Ku, M. G. Blaber, C. A. Mirkin and G. C. Schatz, *Proc. Natl. Acad. Sci. U. S. A.*, 2015, **112**, 10292–10297.

5　L. Sun, H. Lin, D. Park, M. Bourgeois, M. Ross, J. Ku, G. Schatz and C. Mirkin, *Nano Lett.*, 2017, **17**, 2313–2318.

6　S. N. Barnaby, R. V. Thaner, M. B. Ross, K. A. Brown, G. C. Schatz and C. A. Mirkin, *J. Am. Chem. Soc.*, 2015, **137**, 13566–13571.

7　J. Lee, M. Han and C. Mirkin, *Angew. Chem.*, 2007, **119**, 4171–4174.

8　Y. Kang, X. Ye, J. Chen, Y. Cai, R. E. Diaz, R. R. Adzic, E. A. Stach and C. B. Murray, *Journal of the American Chemical Society*, 2013, **135**, 42–45.

9　Y. Kang, X. Ye, J. Chen, L. Qi, R. E. Diaz, V. Doan-Nguyen, G. Xing, C. R. Kagan, J. Li, R. J. Gorte, E. A. Stach and C. B. Murray, *Journal of the American Chemical Society*, 2013, **135**, 1499–1505.

10　E. V. Shevchenko, D. V. Talapin, N. A. Kotov, S. O'Brien and C. B. Murray, *Nature*, 2006, **439**, 55–59.

11　D. Nykypanchuk, M. M. Maye, D. van der Lelie and O. Gang, *Nature*, 2008, **451**, 549–552.

12　R. J. Macfarlane, B. Lee, M. R. Jones, N. Harris, G. C. Schatz and C. A. Mirkin, *Science*, 2011, **334**, 204–208.

13　E. Auyeung, T. I. N. G. Li, A. J. Senesi, A. L. Schmucker, B. C. Pals, M. Olvera de la Cruz and C. A. Mirkin, *Nature*, 2014, **505**, 73–77.

14　T. I. N. G. Li, R. Sknepnek, R. J. Macfarlane, C. A. Mirkin and M. Olvera de la Cruz, *Nano Lett.*, 2012, **12**, 2509–2514.

15　P. Cigler, A. K. R. Lytton-Jean, D. G. Anderson, M. G. Finn and S. Y. Park, *Nat. Mater.*, 2010, **9**, 918–922.

16　A. Ben-Simon, H. Eshet and E. Rabani, *ACS Nano*, 2013, **7**, 978–986.

17　Z. Yang, J. Wei and M. Pileni, *Chem. Mater.*, 2015, **27**, 2152–2157.

18　Y. Kim, R. J. Macfarlane, M. R. Jones and C. A. Mirkin, *Science*, 2016, **351**, 579–582.

19　M. M. Maye, D. Nykypanchuk, D. van der Lelie and O. Gang, *Small*, 2007, **3**, 1678–1682.

20　A. J. Kim, P. L. Biancaniello and J. C. Crocker, *Langmuir*, 2006, **22**, 1991–2001.

21　Y. Wang, Y. Wang, X. Zheng, É. Ducrot, M. G. Lee, G. R. Yi, M. Weck and D. J. Pine, *J. Am. Chem. Soc.*, 2015, **137**, 10760–10766.

22　J. S. Oh, Y. Wang, D. J. Pine and G. R. Yi, *Chem. Mater.*, 2015, **27**, 8337–8344.

23　Y. Wang, Y. Wang, X. Zheng, É. Ducrot, J. S. Yodh, M. Weck and D. J. Pine, *Nat. Commun.*, 2015, **6**, 7253.

24　Y. Zhang, S. Pal, B. Srinivasan, T. Vo, S. Kumar and O. Gang, *Nat. Mater.*, 2015, **14**, 840–847.

25　P. L. Biancaniello, A. J. Kim and J. C. Crocker, *Phys. Rev. Lett.*, 2005, **94**, 94–97.

26　R. Dreyfus, M. E. Leunissen, R. Sha, A. Tkachenko, N. C. Seeman, D. J. Pine and P. M. Chaikin, *Phys. Rev. E*, 2010, **81**, 1–10.

27　L. Di Michele, F. Varrato, J. Kotar, S. H. Nathan, G. Foffi and E. Eiser, *Nat. Commun.*, 2013, **4**, 1–7.

28　S. Angioletti-Uberti, B. M. Mognetti and D. Frenkel, *Nat. Mater.*, 2012, **11**, 518–522.

29　W. B. Rogers and V. N. Manoharan, *Science*, 2015, **347**, 639–642.

30　J. G. Park, S. H. Kim, S. Magkiriadou, T. M. Choi, Y. S. Kim and V. N. Manoharan, *Angew. Chem., Int. Ed.*, 2014, **53**, 2899–2903.

31　R. Ganapathy, S. J. Gerbode and I. Cohen, *Science*, 2010, **327**, 445–448.

32　U. Gasser, E. R. Weeks, A. Schofield, P. N. Pusey and D. A. Weitz, *Science*, 2001, **292**, 258–262.

Soft Matter Accepted Manuscript

33 A. van Blaaderen and P. Wiltzius, *Science*, 1995, **270**, 1177–1179.

34 D. Nykypanchuk, M. M. Maye, D. van der Lelie and O. Gang, *Langmuir*, 2007, **23**, 6305–6314.

35 H. Xiong, D. van der Lelie and O. Gang, *Phys. Rev. Lett.*, 2009, **102**, 015504.

36 M. T. Casey, R. T. Scarlett, W. B. Rogers, I. Jenkins, T. Sinno and J. C. Crocker, *Nat. Commun.*, 2012, **3**, 1209.

37 R. T. Scarlett, M. T. Ung, J. C. Crocker and T. Sinno, *Soft Matter*, 2011, **7**, 1912.

38 Y. Wang, I. C. Jenkins, J. T. McGinley, T. Sinno and J. C. Crocker, *Nat. Commun.*, 2017, **8**, 14173.

39 M. Song, Y. Ding, H. Zerze, M. Snyder and J. Mittal, *Langmuir*, 2018, **34**, 991–998.

40 N. A. Mahynski, H. Zerze, H. W. Hatch, V. K. Shen and J. Mittal, *Soft Matter*, 2017, **13**, 5397–5408.

41 Y. Ding and J. Mittal, *J. Chem. Phys.*, 2014, **141**, 184901.

42 B. M. Mladek, J. Fornleitner, F. J. Martinez-Veracoechea, A. Dawid and D. Frenkel, *Soft Matter*, 2013, **9**, 7342–7355.

43 J. Abraham, S. Buldyrev and N. Giovambattista, *J. Phys. Chem. B*, 2011, **115**, 14229–14239.

44 S. Plimpton, *J. Comput. Phys.*, 1995, **117**, 1–19.

45 J. D. Weeks, D. Chandler and H. C. Andersen, *J. Chem. Phys.*, 1971, **54**, 5237–5247.

46 W. Humphrey, A. Dalke and K. Schulten, *VMD: Visual molecular dynamics*, 1996.

47 A. Stukowski, *Modell. Simul. Mater. Sci. Eng.*, 2010, **18**, 015012.

48 J. Honeycutt and H. Andersen, *J. Phys. Chem.*, 1987, **91**, 4950–4963.

49 A. Stukowski, *Modell. Simul. Mater. Sci. Eng.*, 2012, **20**, 045021.

50 N. Lümmen and T. Kraska, *Modell. Simul. Mater. Sci. Eng.*, 2007, **15**, 319.

51 F. Wang and D. Landau, *Phys. Rev. Lett.*, 2001, **86**, 2050–2053.

52 D. Landau, S.-H. Tsai and M. Exler, *Am. J. Phys.*, 2004, **72**, 1294–1302.

53 H. W. Hatch, N. A. Mahynski and V. K. Shen, *FEASST: Free Energy and Advanced Sampling Simulation Toolkit Version 1.0.0*, 2018, https://doi.org/10.18434/M3S095.

54 I. Jenkins, M. Casey, J. McGinley, J. Crocker and T. Sinno, *Proc. Natl. Acad. Sci. U. S. A.*, 2014, **111**, 4803–4808.

55 F. J. Martinez-Veracoechea, B. M. Mladek, A. V. Tkachenko and D. Frenkel, *Phys. Rev. Lett.*, 2011, **107**, 045902.

56 C. Knorowski, S. Burleigh and A. Travesset, *Phys. Rev. Lett.*, 2011, **106**, 215501.

57 M. E. Leunissen, C. G. Christova, A. Hynninen, C. P. Royall, A. I. Campbell, A. Imhof, M. Dijkstra, R. van Roij and A. van Blaaderen, *Nature*, 2005, **437**, 235–240.

58 A. Travesset, *Proc. Natl. Acad. Sci. U. S. A.*, 2015, **112**, 9563–9567.

59 A. V. Tkachenko, *Proc. Natl. Acad. Sci. U. S. A.*, 2016, **113**, 10269–10274.

60 B. Srinivasan, T. Vo, Y. Zhang, O. Gang, S. Kumar and V. Venkatasubramanian, *Proc. Natl. Acad. Sci. U. S. A.*, 2013, **110**, 18431–18435.